Optical modeling of nanostructures

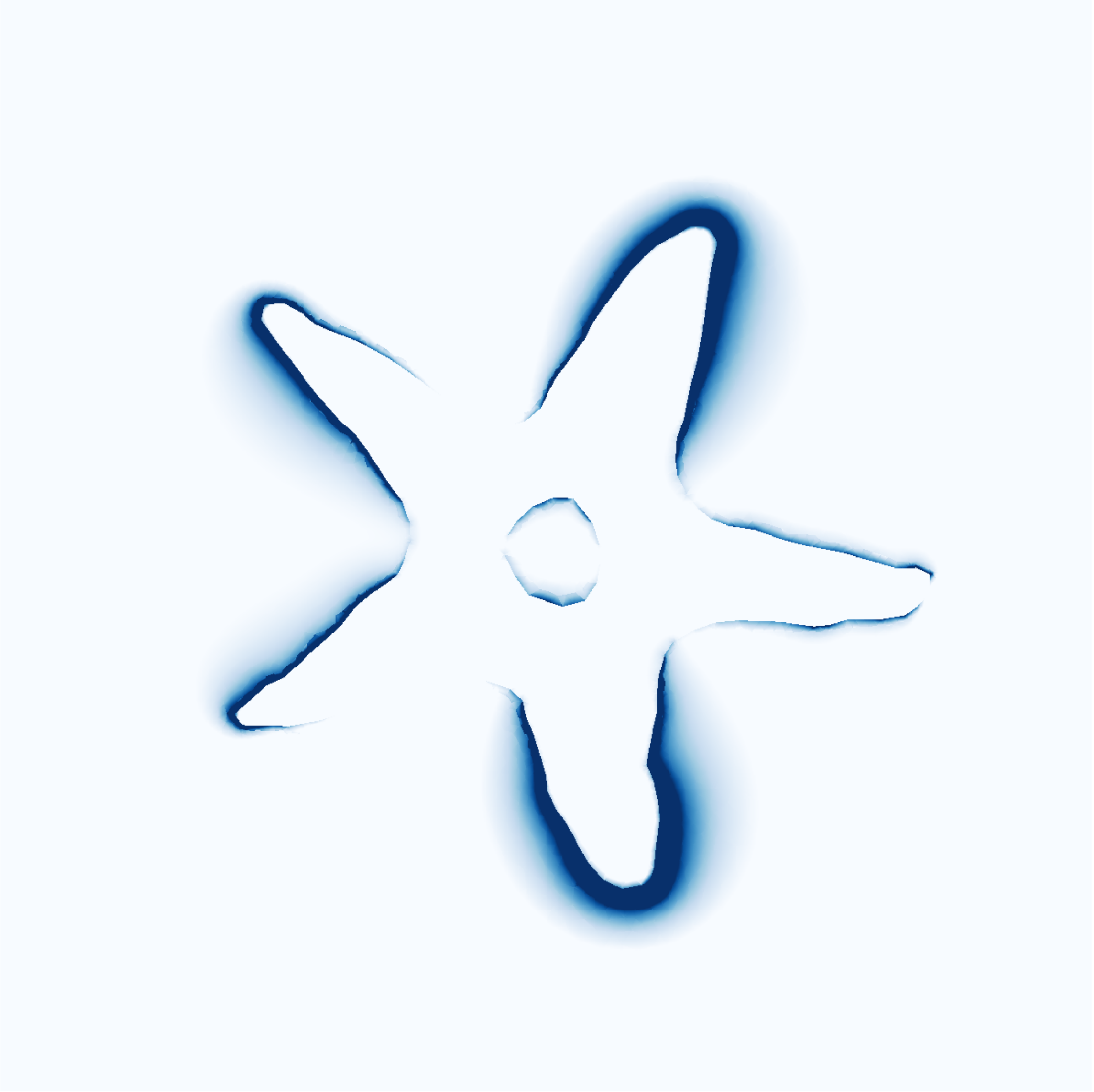

PhD Part A Report

Emil Haldrup Eriksen

20103129

Supervisor: Peter Balling, Søren Peder Madsen

January 2017

Department of Physics and Astronomy
Aarhus University

Contents

Front page illustration: Calculated field enhancement near a gold nanostar fabricated by EBL. The model geometry was constructed in 2D from a top view SEM image using edge detection and extruded to 3D.

1 | Introduction

Solar cells is one of the key technologies in the transition towards an electricity system based on renewable sources. The technology has matured significantly in the last decades, with monocrystalline silicon solar cells recently exceeding 25% in efficiency [1]. As conventional cells approach the Schockley Quessier (SQ) limit [2], exotic concepts enabling efficiencies beyond the SQ limit become increasingly relevant. One such concept is *upconversion*. Upconversion is the process where two, or more, long wavelength (low energy) photons are merged into one short wavelength (high energy) photon. Conventional solar cells are based on a semi conductor material, typically silicon, where the current is generated as an incoming photon (from the sun) excites an electron from the valence band to the conduction band. If the photon energy is not sufficient to bridge the band gap, the process will not occur. For silicon roughly 20% of the energy in the incoming solar radiation is below the band gap (see figure 1.1a) and thus intrinsically lost. However, if an upconverter is integrated into the solar cell, this restriction no longer applies.

This PhD project is part of the SunTune project, which aims at increasing the efficiency of solar cells by tuning the spectrum of the Sun. Currently, upconversion is the process of

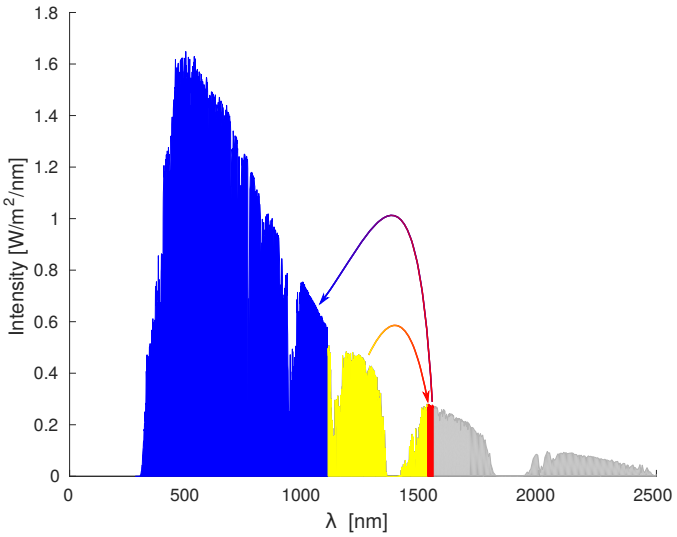

(a) Intensity of solar radiation as a function of wavelength. The colors indicate the part of the spectrum that can be utilized by a silicon solar cell (blue), the part suitable for direct upconversion by Er^{3+} (red) and the part which would would need to be downconverted first (yellow). The arrows indicate the up- (red/blue) and downconversion (yellow/red) steps.

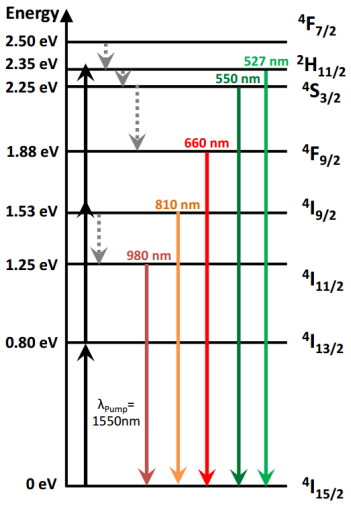

(b) Selected energy levels in Er^{3+}, reproduced from [3]. Radiative transitions are indicated by solid lines while non-radiative transitions are marked by dashed, gray lines.

Figure 1.1: Spectral tuning of solar radiation with upconversion via Er^{3+}. Absorption of 1550 nm photons (below the band gap of silicon) , corresponding to the $^4I_{15/2} \rightarrow ^4 I_{9/2}$ transition, leads to the non-radiative decay $^4I_{9/2} \rightarrow ^4 I_{11/2}$ followed by the emission of a 980 nm photon (above the band gap of silicon) in the radiative $^4I_{11/2} \rightarrow ^4 I_{15/2}$ decay.

main interest, but downconversion will also be studied in the future. The conveniently spaced energy levels of the 4f electronic states in the Er^{3+} ion makes it an ideal candidate for an upconverter material to be used with a silicon solar cell. The concept of spectral tuning with Er^{3+} is illustrated in figure 1.1. The upconversion process is nonlinear, scaling with the intensity to a power $n \geq 1$. At moderate intensities $n \approx 1.6$ [3] implying that the efficiency of the upconversion process can be improved by increasing the intensity. Focusing of the sunlight by conventional lenses is impractical and too expensive, so other options must be explored. Localized surface plasmon resonances (LSPRs) in metal nanoparticles has proven to be a very efficient path to obtain a strong, local field enhancement [4]. Localized surface plasmons are collective excitations of the free electrons in metal nanoparticles. The LSPR frequency depends not only on the geometry of the nanoparticle(s) [5], but also on the dielectric environment [6] and, for small nanoparticles, the material [7]. Manipulation of these parameters allows tuning of the plasmon frequency from visible to mid-infrared [8] implying that a resonance at $\lambda \approx 1500$ nm, so as to match absorption in Er^{3+}, is indeed possible. A key element in the design process for both plasmonic devices and solar cells is *optical modeling*, which has been the main theme in my work so far. When the structures are not too small, quantum effects can be neglected [9], and the problem is reduced to solving Maxwell's equations. A variety of methods have been developed for this purpose, many more than what can be accounted for here. I have mainly worked with the transfer matrix method (TMM) and the finite element method (FEM). As part of this work, contributions have been made to a few papers

- Harish Lakhotiya et al, *Plasmonically enhanced upconversion of 1500 nm light via trivalent Er in a TiO2 matrix* (accepted by APL)
- Sanjay K. Ram et al, *Light-trapping properties of quasi-periodic uniaxial nanowrinkle surface for thin film silicon solar cells* (submitted to ACS Nano)
- Søren Møller et al, *Thickness and wavelength dependence of pulsed femtosecond laser-induced damage thresholds in Ge2Sb2Te5* (in preparation)

Related to the paper on nanowrinkles, I did an oral presentation at the EU PVSEC conference on a combined light trapping and upconversion concept [29]. In addition, the first SunTune paper of my own is currently in preparation

- E. H. Eriksen et al, *Particle-particle interactions in randomly distributed metal nanoparticles, the two particle model* (in preparation)

The progress report is structured as follows. Starting from the Maxwell equations a number of important relations are derived in chapter 2. As a TMM implementation was carried out as part of this work, chapter 3 presents TMM in some detail. Chapter 4 outlines the basic concepts of FEM focusing not on implementation details, but on the application in this project. Finally, a few examples of optical modeling of actual structures are discussed in chapter 5. The main conclusions are summarized in chapter 6 and an outlook on future work is presented.

2 | Maxwell's Equations

In this chapter a number of important equations are derived starting from Maxwell's equations in differential, microscopic form

$$\nabla \cdot \mathbf{E} = \frac{\rho}{\epsilon_0} \tag{2.1}$$

$$\nabla \cdot \mathbf{B} = 0 \tag{2.2}$$

$$\nabla \times \mathbf{E} = -\frac{\partial \mathbf{B}}{\partial t} \tag{2.3}$$

$$\nabla \times \mathbf{B} = \mu_0 \left(\mathbf{J} + \epsilon_0 \frac{\partial \mathbf{E}}{\partial t} \right), \tag{2.4}$$

where $\mathbf{E}/\mathbf{B}$ is the electric/magnetic field, $\rho/\mathbf{J}$ the charge/current density and ϵ_0/μ_0 the vacuum permittivity/permeability.

2.1 Macroscopic form

To describe the macroscopic response of a material, is it helpful define the auxiliary fields

$$\mathbf{D} = \epsilon_0 \mathbf{E} + \mathbf{P} \tag{2.5}$$

$$\mathbf{H} = \frac{1}{\mu_0} \mathbf{B} - \mathbf{M}, \tag{2.6}$$

where $\mathbf{P}$ is the polarization field and $\mathbf{M}$ is the magnetization field. The bound charge/current densities are related to the auxiliary fields as

$$\rho_{bnd} = -\nabla \cdot \mathbf{P} \tag{2.7}$$

$$\mathbf{J}_{bnd} = \nabla \times \mathbf{M} + \frac{\partial \mathbf{P}}{\partial t} = \mathbf{J}_{mag} + \mathbf{J}_{pol}. \tag{2.8}$$

The total charge/current density is the sum of the bound part and any *free* contributions. With these definitions, Maxwell's equations can be cast into their *macroscopic* form

$$\nabla \cdot \mathbf{D} = \rho_{free} \tag{2.9}$$

$$\nabla \cdot \mathbf{B} = 0 \tag{2.10}$$

$$\nabla \times \mathbf{E} = -\frac{\partial \mathbf{B}}{\partial t} \tag{2.11}$$

$$\nabla \times \mathbf{H} = \mathbf{J}_{free} + \frac{\partial \mathbf{D}}{\partial t}. \tag{2.12}$$

Of particular importance are time harmonic fields, e.g. fields of the form[1]

$$\mathbf{V}(\mathbf{r}, t) = \mathbf{V}(\mathbf{r}) e^{-i\omega t}. \tag{2.13}$$

[1] Engineers tend to use the opposite sign convention in the exponential function.

Inserting the time harmonic ansatz, equation (2.13), for the **E**, **D**, **B**, and **H** fields into equations (2.9) to (2.12), their time harmonic form is obtained

$$\nabla \cdot \mathbf{D} = \rho_{free} \tag{2.14}$$
$$\nabla \cdot \mathbf{B} = 0 \tag{2.15}$$
$$\nabla \times \mathbf{E} = iw\mathbf{B} \tag{2.16}$$
$$\nabla \times \mathbf{H} = \mathbf{J}_{free} - i\omega\mathbf{D}. \tag{2.17}$$

Before the macroscopic Maxwell equations can be applied, a description of the material response is required. The equations specifying the response are called *constitutive relations*. If the response is linear, the constitutive relation are

$$\mathbf{D} = \epsilon\mathbf{E}, \quad \mathbf{H} = \frac{1}{\mu}\mathbf{B}, \tag{2.18}$$

where ϵ/μ is the permittivity/permeability of the material. In optics it is common to work with the refractive index n rather than ϵ and μ. Their relation is

$$\epsilon\mu = (\epsilon_0\mu_0)\,\epsilon_r\mu_r = \left(\frac{n}{c_0}\right)^2, \tag{2.19}$$

where ϵ_r/μ_r is the relative permittivity/permeability and c_0 the speed of light in vacuum.

2.2 The wave equation

Maxwell's equations, in the form equations (2.14) to (2.17), are a set of coupled, first-order differential equations. They can be decoupled by taking the curl of equation (2.16) and inserting equation (2.17),

$$\nabla \times \left(\frac{1}{\mu}\nabla \times \mathbf{E}\right) = i\omega\left(\nabla \times \mathbf{H}\right) = i\omega\left(\mathbf{J}_{free} - i\omega\mathbf{D}\right) \tag{2.20}$$

Assuming that no external currents are present so that $\mathbf{J}_{free}$ is solely due to a material response following Ohms law, equation (2.20) can be rewritten as

$$\nabla \times \left(\frac{1}{\mu}\nabla \times \mathbf{E}\right) = i\omega\left(\sigma - i\omega\epsilon\right)\mathbf{E} = \epsilon_0\left(\epsilon_r + i\frac{\sigma}{\omega\epsilon_0}\right)\omega^2\mathbf{E}. \tag{2.21}$$

Defining the the complex permittivity

$$\tilde{\epsilon} = \epsilon_0\left(\epsilon_r + i\frac{\sigma}{\omega\epsilon_0}\right) \tag{2.22}$$

so as to take into account the combined effect of bound charges and conduction current [10], equation (2.21) is reduced to

$$\nabla \times \left(\frac{1}{\mu}\nabla \times \mathbf{E}\right) - \tilde{\epsilon}\omega^2\mathbf{E} = 0. \tag{2.23}$$

This is the wave equation for the electric field. It will be the defining differential equation for the formulation of all boundary value problems in this work.

2.3 Assumptions

In this work, all media will be assumed isotropic, non-magnetic and the displacement field will be assumed linear. Hence the relevant constitutive relations are

$$\mathbf{D} = \epsilon \mathbf{E}, \quad \mathbf{H} = \frac{1}{\mu_0}\mathbf{B}, \tag{2.24}$$

with ϵ being a (complex) scalar. If the permittivity is complex (conductor), the refractive index will be complex too. Since the non-magnetic assumption implies $\mu_r = 1$, the relation between permittivity and refractive index, equation (2.19), simply becomes

$$\tilde{n} = \sqrt{\tilde{\epsilon}_r} = n + i\kappa. \tag{2.25}$$

It is assumed that no free charges/currents are present except for those accounted for by the complex permittivity. Also, all fields are assumed time harmonic and complex notation is used. To get the field value at time t, multiply by $e^{-i\omega t}$ and take the real part.

2.4 Boundary conditions

Boundary conditions for the interfaces between different media can be derived directly from Maxwell's equations. The standard approach is to convert them into integral form by applying the divergence theorem and Stokes's theorem, after which they are applied to an infinitesimal Gaussian pillbox at the boundary surface between the two media. A derivation can be found in e.g. [11]. The result reads

$$(\mathbf{D}_2 - \mathbf{D}_1) \cdot \hat{\mathbf{n}} = \sigma_s \tag{2.26}$$

$$(\mathbf{B}_2 - \mathbf{B}_1) \cdot \hat{\mathbf{n}} = 0 \tag{2.27}$$

$$\hat{\mathbf{n}} \times (\mathbf{E}_2 - \mathbf{E}_1) = 0 \tag{2.28}$$

$$\hat{\mathbf{n}} \times (\mathbf{H}_2 - \mathbf{H}_1) = \mathbf{K}_s \tag{2.29}$$

where $\hat{\mathbf{n}}$ is the surface normal vector and $\sigma_s/\mathbf{K}_s$ the surface charge/current density.

2.5 Polarization conventions

In this work, the main problem of interest is plane waves,

$$\mathbf{E}(\mathbf{r}) = \mathbf{E}_0 e^{i\mathbf{k}\cdot\mathbf{r}}, \tag{2.30}$$

incident upon a sample. The sample plane is chosen as the xy-plane so that a wave propagating along the z-axis will be normally incident. The wave vector is chosen as

$$\mathbf{k}_{f/b} = \tilde{n}\left(\pm\hat{\mathbf{z}}\cos\theta + \hat{\mathbf{x}}\sin\theta\right)k_0, \tag{2.31}$$

where θ is the polar angle with respect to the sample surface normal $\hat{\mathbf{n}}$ and the indices f/b indicate forward/backward propagation (for which the $\pm$ symbol should be interpreted as $+/-$ respectively). With these definitions the *plane of incidence*, spanned by $\hat{\mathbf{n}}$ and $\mathbf{k}$, will be the xz-plane. An arbitrary polarization state can be decomposed into components with the **E**-field perpendicular (s-polarization) and parallel (p-polarization) to the plane

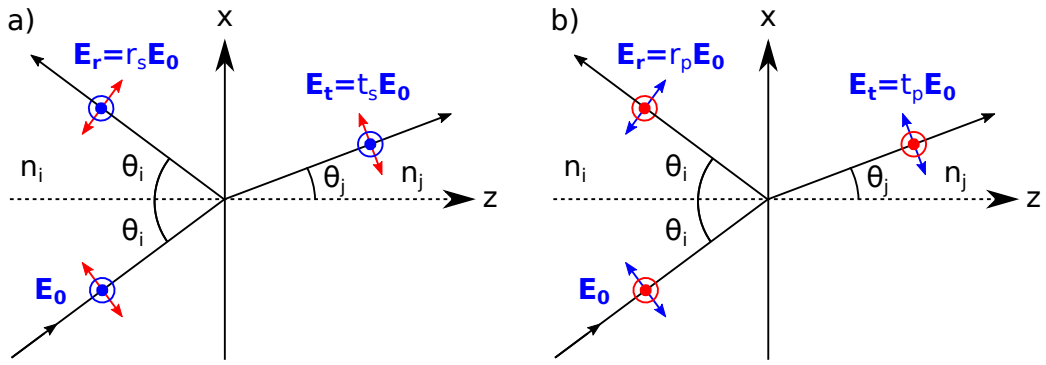

Figure 2.1: Plane wave incident on an interface between two different media. Directions of the **E** (blue) and **H** (red) fields are indicated for (a) s- and (b) p-polarization. The amplitudes of the incident $\mathbf{E}_0$, reflected $\mathbf{E}_r$ and transmitted $\mathbf{E}_t$ waves are related through the complex Fresnel coefficients (see section 3.1).

of incidence as illustrated in figure 2.1. In the case of s-polarization, the **E**-field will be in the y-direction. The **H**-field can be derived from the **E**-field using equation (2.16),

$$\mathbf{H} = \frac{1}{i\omega\mu_0}(\nabla \times \mathbf{E}) = \frac{E}{\omega\mu_0}(-\hat{\mathbf{x}}k_z + \hat{\mathbf{z}}k_x) = \frac{E\tilde{n}}{c_0\mu_0}(\mp\hat{\mathbf{x}}\cos\theta + \hat{\mathbf{z}}\sin\theta)\,. \tag{2.32}$$

For p-polarization, the **H**-field is in the y-direction. Equation (2.17) allows the evaluation of the **E**-field from the **H**-field,

$$\mathbf{E} = \frac{-1}{i\omega\epsilon}(\nabla \times \mathbf{H}) = \frac{-H}{\omega\epsilon_0\tilde{n}^2}(-\hat{\mathbf{x}}k_z + \hat{\mathbf{z}}k_x) = \frac{-Hc_0\mu_0}{\tilde{n}}(\mp\hat{\mathbf{x}}\cos\theta + \hat{\mathbf{z}}\sin\theta)\,. \tag{2.33}$$

Writing out the explicit expressions for the **E**- and **H**-fields, one must decide whether the sign of the backward traveling wave should be based on the relative phase of (1) the **E**-field or (2) the **H**-field. For s-polarization there is agreement in the literature to choose convention (1),

$$\mathbf{E} = +E\hat{\mathbf{y}}, \quad \mathbf{H} = \frac{\tilde{n}E}{c_0\mu_0}(\mp\hat{\mathbf{x}}\cos\theta + \hat{\mathbf{z}}\sin\theta) \quad \text{(s-pol)}. \tag{2.34}$$

For p-polarization on the other hand, the textbooks are split almost evenly [12]. Since in this work the **E**-field is of main interest, convention (1) will be adapted also for p-polarization[2],

$$\mathbf{H} = \pm H\hat{\mathbf{y}}, \quad \mathbf{E} = \frac{Hc_0\mu_0}{\tilde{n}}(\hat{\mathbf{x}}\cos\theta \mp \hat{\mathbf{z}}\sin\theta) \quad \text{(p-pol)}. \tag{2.35}$$

When $\tilde{n}$ is constant (which is true everywhere except at the boundaries), the p-polarized field can be expressed in terms of the amplitude of the **E**-field as

$$\mathbf{H} = \pm\frac{E\tilde{n}}{c_0\mu_0}\hat{\mathbf{y}}, \quad \mathbf{E} = E(\hat{\mathbf{x}}\cos\theta \mp \hat{\mathbf{z}}\sin\theta) \quad \text{(p-pol)}. \tag{2.36}$$

Since equation (2.36) is not valid at the boundaries, equation (2.35) must be applied when boundary conditions are evaluated.

[2] As a side bonus, this choice implies $r_s = r_p$ (see section 3.1) at normal incidence in accordance with expectation (at normal incidence s-/p-polarization are physically equivalent).

3 | Transfer Matrix Method(s)

In this chapter the standard transfer matrix method (TMM) is outlined along with a number of extensions. The incentive for presenting TMM in detail is twofold. First, the TMM method is used to calculate the background field used in the scattered field calculations presented in chapter 4. Secondly, TMM provides the foundation of the angular TMM extensions [13, 14], based on which a future publication is planned.

3.1 Fresnel equations

The Fresnel equations describe the reflection and transmission of electromagnetic waves at a planer interface as shown in figure 2.1. Applying Maxwells equations, the complex coefficients of transmission/reflection for the electric field can be derived

$$t_s = \frac{2\tilde{n}_i \cos\theta_i}{\tilde{n}_i \cos\theta_i + \tilde{n}_j \cos\theta_j}, \quad r_s = \frac{\tilde{n}_i \cos\theta_i - \tilde{n}_j \cos\theta_j}{\tilde{n}_i \cos\theta_i + \tilde{n}_j \cos\theta_j} \tag{3.1}$$

$$t_p = \frac{2\tilde{n}_i \cos\theta_i}{\tilde{n}_j \cos\theta_i + \tilde{n}_i \cos\theta_j}, \quad r_p = \frac{\tilde{n}_i \cos\theta_j - \tilde{n}_j \cos\theta_i}{\tilde{n}_j \cos\theta_i + \tilde{n}_i \cos\theta_j}. \tag{3.2}$$

along with Snell's law

$$\tilde{n}_i \sin\theta_i = \tilde{n}_j \sin\theta_j. \tag{3.3}$$

The energy reflectance/transmittance is the ratio between the z-components of the incident and the reflected/transmitted intensity. They are related to r, t as

$$R = |r|^2, \quad T = |t|^2\gamma \tag{3.4}$$

where the polarization dependent factor γ is

$$\gamma_s = \frac{\mathrm{Re}\left[\left(n_j \cos\theta_j\right)^*\right]}{\mathrm{Re}\left[\left(n_i \cos\theta_i\right)^*\right]}, \quad \gamma_p = \frac{\mathrm{Re}\left[n_j^* \cos\theta_j\right]}{\mathrm{Re}\left[n_i^* \cos\theta_i\right]}. \tag{3.5}$$

3.2 The transfer matrix method

The standard transfer matrix method treats a monochromatic, coherent, plane wave incident upon stack of planar, homogeneous layers. At any point in the stack, the electric field can be represented as a super position of a forward and a backward traveling wave,

$$\mathbf{E}(\mathbf{r}) = \mathbf{E}_f e^{i\mathbf{k}_f \cdot \mathbf{r}} + \mathbf{E}_b e^{i\mathbf{k}_b \cdot \mathbf{r}}. \tag{3.6}$$

For notational convenience, the amplitude of the forward/backward propagating wave will be denoted v and w respectively. Expressing the amplitudes as a vector, the traversal of the stack can be expressed as a matrix equation

$$\begin{pmatrix} v_0 \\ w_0 \end{pmatrix} = \mathbf{S} \begin{pmatrix} v \\ w \end{pmatrix}, \tag{3.7}$$

where **S** is the stack *scattering matrix*. As a simple example, consider a wave traveling through a layer indexed by i. The forward traveling wave is shifted in phase by

$$\beta_i = \left(\frac{2\pi d_i n_i}{\lambda_0}\right)\cos\theta_i \tag{3.8}$$

where the (complex) angle θ_i is calculated from Snells law, equation (3.3). Likewise the backward traveling wave is shifted by $-\beta_i$,

$$v = v_0 e^{i\beta} \tag{3.9}$$

$$w = w_0 e^{-i\beta}. \tag{3.10}$$

Expressed in the form of equation (3.7), the *layer propagation matrix* is

$$\mathbf{L}_i = \mathbf{L}(\beta_i) = \begin{pmatrix} \exp(-\beta_i) & 0 \\ 0 & \exp(\beta_i) \end{pmatrix}. \tag{3.11}$$

Next, consider an interface between layers i and j. By matching the amplitudes at each side of the interface, the relations

$$v = v_0 t_{i,j} + w r_{j,i} \tag{3.12}$$

$$w_0 = w t_{j,i} + v_0 r_{i,j} \tag{3.13}$$

are obtained with $r_{i,j}$ and $t_{i,j}$ being the (complex) Fresnel coefficients derived in section 3.1 when going from layer i to layer j. Rearranging terms,

$$v_0 = \frac{1}{t_{i,j}}\left(v - w r_{j,i}\right) \tag{3.14}$$

$$w_0 = \frac{1}{t_{i,j}}\left(w(t_{i,j}t_{j,i} - r_{i,j}r_{j,i}) + v r_{i,j}\right). \tag{3.15}$$

Expressed in the form of equation (3.7), the *interface matrix* is

$$\mathbf{I}_{i,j} = \frac{1}{t_{i,j}}\begin{pmatrix} 1 & -r_{j,i} \\ r_{i,j} & t_{i,j}t_{j,i} - r_{i,j}r_{j,i} \end{pmatrix}. \tag{3.16}$$

The scattering matrix for the an arbitrary layer stack is constructed by matrix multiplication of the element matrices. For a stack of m layers

$$\mathbf{S} = \mathbf{I}_{0,1}\mathbf{L}_1\mathbf{I}_{1,2}\ldots\mathbf{L}_{m-1}\mathbf{I}_{m-1,m}. \tag{3.17}$$

3.2.1 Reflection/transmission coefficients

The (complex) reflection/transmission coefficients of the complete stack can be derived directly from the scattering matrix. First, consider light incident from the left. In this case, the wave traveling backward on the right side of the structure (w) must be zero. Dividing by the incident field v_0, the matrix equation reads

$$\begin{pmatrix} 1 \\ r \end{pmatrix} = \mathbf{S}\begin{pmatrix} t \\ 0 \end{pmatrix}, \tag{3.18}$$

where r/t denote the reflectance/transmittance coefficients defined as

$$r = \frac{w_0}{v_0} = \frac{S_{21}}{S_{11}}, \quad t = \frac{v}{v_0} = \frac{1}{S_{11}}. \tag{3.19}$$

Next, consider light incident from the right. In this case the wave traveling forward on the left side of the structure (v_0) must be zero. Dividing by the incident field w, the matrix equation reads

$$\begin{pmatrix} 0 \\ t' \end{pmatrix} = \mathbf{S} \begin{pmatrix} r' \\ 1 \end{pmatrix}, \tag{3.20}$$

where r'/t' denote the back-reflectance/transmittance coefficients defined as

$$r' = \frac{v}{w} = -\frac{S_{12}}{S_{11}}, \quad t' = \frac{w_0}{w} = \frac{\det \mathbf{S}}{S_{11}}. \tag{3.21}$$

Combining equations (3.19) and (3.21), the scattering matrix can be expressed in terms of the reflection/transmission coefficients,

$$\mathbf{S} = \frac{1}{t} \begin{pmatrix} 1 & -r' \\ r & tt' - rr' \end{pmatrix}. \tag{3.22}$$

Note the similarity with equation (3.16). It implies that the scattering matrix can be interpreted as an *effective* interface matrix for the complete structure.

3.3 Incoherence

In the standard transfer matrix method (TMM), the light is assumed to be perfectly coherent. While this can be a reasonable assumption some light/structure combinations, the assumption is not generally true. If the layer thickness is large compared to the coherence length of the light, the coherent assumption breaks down. Even if this is not the case, imperfect interfaces and/or variations in layer thicknesses can cause loss of coherence. A number of different approaches have been proposed to extend TMM to deal with incoherence. This section provides a brief overview.

3.3.1 Phase averaging method

Loss of coherence basically means that the relative phase information between successive reflections is lost. This effect can be emulated in the TMM simulations by adding a random offset δ to the phase shift β_i obtained when a layer is traversed,

$$\beta_i \to \beta_i + \delta, \quad \delta \in [0 : \delta_{max}]. \tag{3.23}$$

Evaluating the relevant quantities, typically R and T, for a number N of offsets, the incoherent values are obtained by calculating the average value [15],

$$T_{PAM} = \sum_{i=1}^{N} \frac{T_i}{N}. \tag{3.24}$$

The number N should be large enough that convergence is obtained. A faster convergence can be obtained by choosing the values of δ equally spaced rather than randomly [16].

By varying the parameter δ_{max} in equation (3.23) between 0 (perfect coherence) and π (complete incoherence), semi-coherence can be simulated too. Example calculations are shown in figure 3.1. A disadvantage of the phase averaging method (PAM) is that the computation time is increased by a factor of N. How large a value of N is needed depends of the problem, but typically $N \approx 30$ is required [15] when the values of δ are chosen equidistantly.

3.3.2 Gaussian filter method

Real light sources are not perfectly coherent, nor monochromatic. The coherence length l of a wave train is related to the line width $\Delta\lambda$ as [17]

$$\Delta\lambda = \frac{\lambda^2}{l}. \tag{3.25}$$

Assume that the the relevant quantities, typically R and T, have been evaluated using TMM across some spectral range. The final line width, $\Delta\lambda$, of the light source can then be taken into account by applying a Gaussian filter [18]

$$g(\lambda) = \frac{1}{\sqrt{2\pi}\sigma} e^{-\frac{\lambda^2}{2\sigma^2}} \text{ with } \sigma = \frac{2}{\pi}\frac{\lambda^2}{l}. \tag{3.26}$$

The limit $l \to \infty$ corresponds to perfect coherence (e.g. the filter does nothing), while the limit $l \to 0$ implies complete incoherence. By varying l, semi-coherence can be simulated [19]. Example calculations are shown in figure 3.2. In terms of computation, a large overhead is introduced if the target variable is the response at a single wavelength only. However, if a frequency sweep is needed anyway, only a minor overhead (the scan must be extended in each end) is present.

3.3.3 Absolute square method

While the methods presented in section 3.3.2 and section 3.3.1 are direct extensions of TMM, the absolute square method (ASM) is different in that it considers the amplitude(s) of the intensity field $U = |E^2|$ rather than the electric field [20]. The basic idea, however, is the same. The equivalent of equation (3.7) is

$$\begin{pmatrix} V_0 \\ W_0 \end{pmatrix} = \bar{\mathbf{S}} \begin{pmatrix} V \\ W \end{pmatrix} \tag{3.27}$$

where V, W are the amplitudes of the forward/backward propagating intensity field and a bar is used to distinguish the incoherent scattering matrix from the coherent one. Similarly, by making the the substitutions $r \to \bar{r} \equiv |r|^2$ and $t \to \bar{t} \equiv |t|^2$ in equation (3.22), the incoherent scattering matrix is obtained

$$\bar{\mathbf{S}} = \frac{1}{\bar{t}} \begin{pmatrix} 1 & -\bar{r}' \\ \bar{r} & \bar{t}\bar{t}' - \bar{r}\bar{r}' \end{pmatrix} = \begin{pmatrix} |S_{11}|^2 & -|S_{12}|^2 \\ |S_{21}|^2 & \frac{|det(\mathbf{S})|^2 + |S_{12}S_{21}|^2}{|S_{11}|^2} \end{pmatrix}. \tag{3.28}$$

At the last equality sign, equations (3.19) and (3.21) were used to relate r, t to the corresponding coherent scattering matrix $\mathbf{S}$. Equation (3.28) makes it possible to calculate the

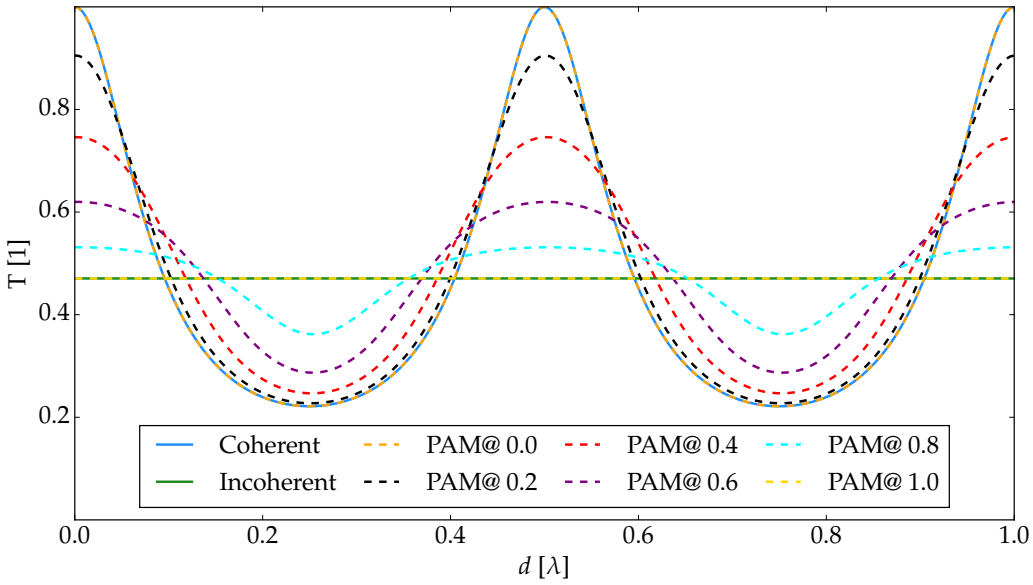

Figure 3.1: Transmittance from a Fabry-Perot etalon (glass slab) with $n = 4$ as a function of thickness in units of $\lambda = \lambda_0/n$. The coherent calculations predict perfect transmittance when d equals an integer times $\lambda/2$ due to destructive interference between front and backside reflections. The incoherent calculations predict a constant transmittance. Applying PAM, results for semi-coherent light can be obtained. For the PAM results the number in the legend denotes δ_{max} in units of π.

incoherent scattering matrix from the its coherent equivalent. From equation (3.11) the incoherent layer propagation matrix is obtained

$$\bar{\mathbf{L}}_i = \bar{\mathbf{L}}(\beta_i) = \begin{pmatrix} |\exp(-\beta_i)|^2 & 0 \\ 0 & |\exp(\beta_i)|^2 \end{pmatrix}. \tag{3.29}$$

The incoherent interface matrix follows from equation (3.16),

$$\bar{\mathbf{I}}_{i,j} = \frac{1}{|t_{i,j}|^2} \begin{pmatrix} 1 & |r_{j,i}|^2 \\ |r_{i,j}|^2 & |t_{i,j}t_{j,i}|^2 - |r_{i,j}r_{j,i}|^2 \end{pmatrix}. \tag{3.30}$$

As in TMM, the scattering matrix for an arbitrary (now incoherent) layer stack is constructed by matrix multiplication of the element matrices,

$$\bar{\mathbf{S}} = \bar{\mathbf{I}}_{0,1}\bar{\mathbf{L}}_1\bar{\mathbf{I}}_{1,2}\ldots\bar{\mathbf{L}}_{m-1}\bar{\mathbf{I}}_{m-1,m}. \tag{3.31}$$

The analysis leading the to front/back reflection and transmission coefficient is practically equivalent to the TMM case, the results are

$$\bar{r} = \frac{W_0}{V_0} = \frac{\bar{S}_{21}}{\bar{S}_{11}}, \quad \bar{t} = \frac{V}{V_0} = \frac{1}{\bar{S}_{11}} \tag{3.32}$$

$$\bar{r}' = \frac{V}{W} = -\frac{\bar{S}_{12}}{\bar{S}_{11}}, \quad \bar{t}' = \frac{W_0}{W} = \frac{\det\bar{\mathbf{S}}}{\bar{S}_{11}}. \tag{3.33}$$

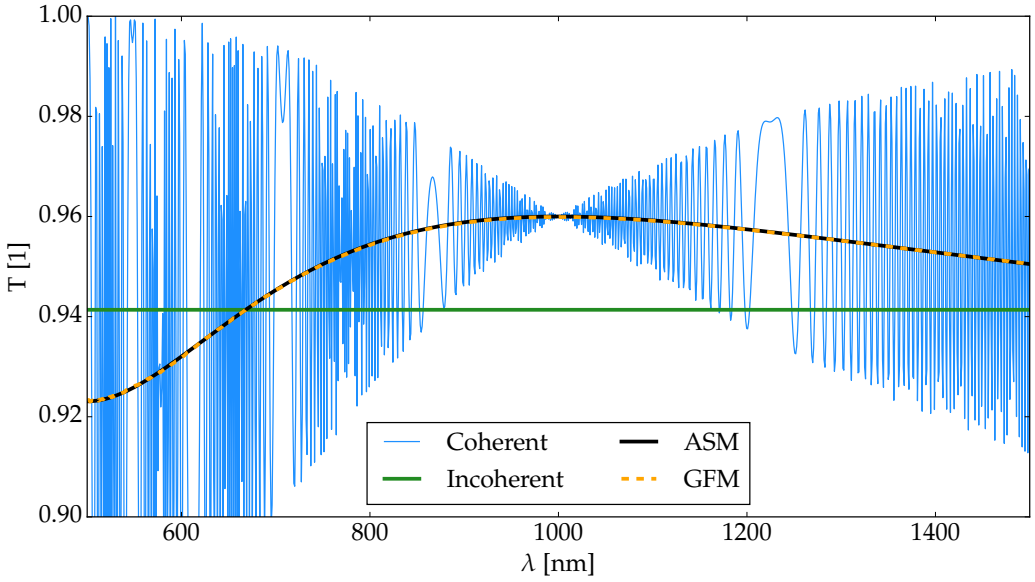

Figure 3.2: Transmittance from a 0.5 mm glass substrate, $n_{subst} = 1.5$, with an anti reflection (AR) coating ($n_{AR} = \sqrt{n_{subst}}$, design wavelength 1000 nm) as a function of wavelength. The coherent calculation show strong oscillations due to interference with the backside reflection from the thick glass substrate, while the incoherent calculation predicts a constant transmittance. Applying ASM, a calculation was carried out treating the AR coating coherently and the substrate incoherently. The result agrees perfectly with the result obtained by GFM assuming a coherence length of 10 μm.

with equation (3.4) replaced by

$$R = \bar{r}, \quad T = \bar{t}\gamma. \tag{3.34}$$

In the case of coherent layer(s) embedded inside the incoherent stack, equation (3.28) can be applied to the scattering matrix of the coherent layer(s) to obtain the *effective incoherent interface matrix*. The mixed coherent/incoherent case is thus reduced to the incoherent one. Note that this trick allows ASM to treat an arbitrary stack of mixed coherent and incoherent layers. Since ASM supports direct evaluation of the case of complete incoherence, it serves as an obvious benchmark for the convergence of the of PAM and GFM towards the incoherent limit. Example calculations are included in figures 3.1 and 3.2.

3.4 Implementation

Numerous implementations of TMM exist. Among the most powerful, both in terms of usability and flexibility, is the Python package *tmm* by Steve Byrnes [12]. However, driven by (1) the need to interface with other programs (e.g. COMSOL) and (2) the need to extend the basic TMM functionally, a new implementation was forged as a part of this work. The implementation is written in Python (object oriented) and it includes all of the TMM extensions discussed in this chapter. An alpha version is available from pypi under the package name *tmmpy*. Figures 3.1 and 3.2 were created using *tmmpy*.

4 | The Finite Element Method

The finite element method (FEM) is a numerical technique for obtaining approximate solutions to boundary value problems. FEM has been around since the 1940s, and today the method is applied in a variety of fields including structural analysis, fluid dynamics and electromagnetics. Many great books are available on the subject, both legible [21] and comprehensive [22]. In this chapter a brief introduction to the basic principles of FEM is given and the differential equations and boundary conditions used in this work are presented.

4.1 Basic principle(s)

Modern FEM implementations are based on either the Ritz variational method or the Galerkin method. Both are classical methods for solving boundary value problems. The basic idea is to expand the unknown solution in some basis after which the boundary value problem is converted into a linear system of equations for the (unknown) expansion coefficients. A very important step in the process is the choice of basis. For most one dimensional problems it is possible to find appropriate basis functions, but for problems in two and three dimensions such functions might not be readily available. The core idea of FEM is to overcome this obstacle by splitting the domain into smaller parts called *elements*. Instead of using complicated basis functions defined on the complete domain Ω, simple basis functions (typically low order polynomials) defined on each element $\Omega_n \in \Omega$ are used. Applying the Galerkin or the Ritz method for each element and summing over all elements, a linear system of equations is obtained. The process of constructing this system, including the enforcement of boundary conditions, is referred to as *assembly*. The FEM can thus be summarized in three main steps

- **Discretization** of the domain into elements
- **Assembly** of the linear system of equations
- **Solution** of the system

Since an actual FEM implementation has not been carried out as part of this work, details on the assembly process is beyond the scope of this progress report. Instead the reader is referred to [22]. The discretization and solution steps on the other hand are performance critical and must be hand tuned. A few comments of these steps are provided in the following paragraphs.

4.1.1 Discretization

The discretization (or *meshing*) step is of uttermost importance. It affects the required memory, the computation time and the accuracy of the solution. In general terms, a higher mesh resolution improves the accuracy of solution at the cost of increased memory consumption and computation time. However, the *mesh quality* is just as important.

A higher mesh quality implies obtaining a higher accuracy without increasing the number of mesh elements. The generation of high quality meshes is a science of its own, but typical tricks include (1) enforcing physical boundaries in the mesh construction and (2) increasing the number of elements in regions where gradients are expected to be high.

For the simulation of electric fields, the so-called Nédélec elements are preferred. They enforce tangential continuity across element interfaces, e.g equation (2.28) is enforced automatically. In addition, as the mesh should always be fine enough to resolve the field oscillation, at least 6 elements per wavelength should be present. In this work the COMSOL mesh generator was used to generate tetrahedral meshes of second order Nédélec elements. Since the wavelength depends linearly on the refractive index n, the mesh resolution was scaled accordingly as illustrated in figure 4.1a. Additionally, as illustrated in figure 4.1b, the mesh resolution was increased along the boundary of metal nanoparticles, as a high field gradient is expected in this region.

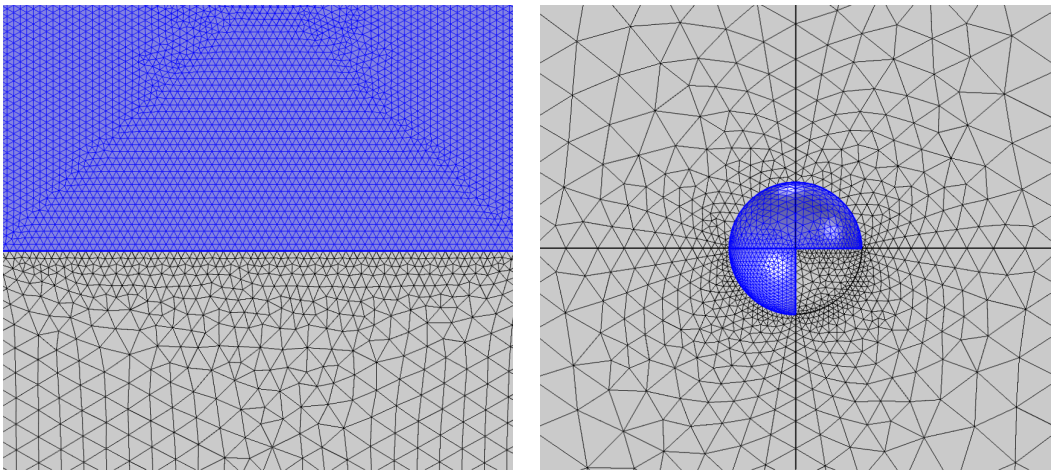

(a) Interface between air and a naked silicon substrate. Due to the high value of the n for silicon, the mesh is much more dense in the substrate (blue).

(b) Gold sphere in vacuum. As a high field gradient is expected close to the sphere, the mesh resolution is increased at the sphere surface (blue).

Figure 4.1: Examples of custom mesh generation.

Solution

Solving the linear system of equations is the final and typically the most time consuming step. The FEM system matrix is sparse and often symmetric. The solver should always be chosen to exploit such properties. The process of solving large, sparse, linear systems of equations is a standard linear algebra operation for which efficient solvers are freely available [23]. Two classes exist, *direct* and *iterative* solvers. Direct solvers solve the problem in one step, often by LU decomposition. The advantage of direct solvers are their stability, while the trade-off is a high memory consumption. For very large problems, the memory consumption might exceed the available amount of RAM, and one is forced to employ an iterative solver instead. Iterative solvers start from some solution guess and refines it iteratively. The advantage of iterative solvers is the reduced memory usage, but it comes at the cost of stability. Not all iterative solvers arrive at the same solution, and often they do not even converge.

4.2 Scattered field formulation

The wave equation, equation (2.23), was derived in section 2.2. It is the core differential equation for all FEM calculations carried out in this work. Since it implies solving for the total field, it is referred to as the *full field formulation*.

A slightly different approach designed specifically for scattering problems is the *scattered field formulation*. To illustrate the basic idea, consider a structure with some scattering element(s). In the absence of the scattering element(s), the background structure is characterized by some permittivity function $\tilde{\epsilon}_B$. The background field $\mathbf{E}_B$ is then defined as the solution to the wave equation

$$\nabla \times \left(\frac{1}{\mu_0} \nabla \times \mathbf{E}_B \right) - \tilde{\epsilon}_B \omega^2 \mathbf{E}_B = 0. \tag{4.1}$$

Applying the superposition principle, the full field $\mathbf{E}$ can be written as

$$\mathbf{E} = \mathbf{E}_B + \mathbf{E}_S \tag{4.2}$$

where $\mathbf{E}_S$ is the scattered field due to the presence of the scattering element. Inserting equation (4.2) into equation (2.23) and solving for the scattered field, the *scattered field formulation* is recovered

$$\nabla \times \left(\frac{1}{\mu_0} \nabla \times \mathbf{E}_S \right) - \tilde{\epsilon} \omega^2 \mathbf{E}_S = -\nabla \times \left(\frac{1}{\mu_0} \nabla \times \mathbf{E}_B \right) + \tilde{\epsilon} \omega^2 \mathbf{E}_B. \tag{4.3}$$

In the scattered field formulation, the field which is solved for the is not the total field $\mathbf{E}$, but the scattered field $\mathbf{E}_S$. Contrary to the full field formulation, the source term (the right hand side) is not zero. To clarify the meaning of the source term, equation (4.1) is substituted into equation (4.3),

$$\nabla \times \left(\frac{1}{\mu_0} \nabla \times \mathbf{E}_S \right) - \tilde{\epsilon} \omega^2 \mathbf{E}_S = \left(\tilde{\epsilon} - \tilde{\epsilon}_B \right) \omega^2 \mathbf{E}_B. \tag{4.4}$$

From equation (4.4) it is clear that the background field acts as a source of excitation in regions where $\mathbf{E}_B \neq 0$ and $\tilde{\epsilon} \neq \tilde{\epsilon}_B$.

4.3 Boundary conditions

To complete the formulation of a boundary value problem, boundary conditions (BCs) must be supplied in addition to the differential equation. The basic principles of the BCs used in this work are outlined in this section.

4.3.1 Perfect Conductor

For a perfect electric/magnetic conductor (PEC/PMC), the internal electric/magnetic field is zero. In this case, equations (2.26) to (2.29) are reduced to

$$\mathbf{D} \cdot \hat{\mathbf{n}} = \sigma_s \quad \text{(PEC)} \tag{4.5}$$

$$\mathbf{E} \times \hat{\mathbf{n}} = 0 \quad \text{(PEC)} \tag{4.6}$$

$$\mathbf{B} \cdot \hat{\mathbf{n}} = 0 \quad \text{(PMC)} \tag{4.7}$$

$$\mathbf{H} \times \hat{\mathbf{n}} = \mathbf{K}_s \quad \text{(PMC)}, \tag{4.8}$$

where $\sigma_s/\mathbf{K}_s$ is the induced charge/current on the surface. The PEC BC can be used to approximate metallic objects, the advantage being to avoid meshing the internals of the object. Additionally, the PEC/PMC BC can be used to represent symmetry planes for the electric/magnetic field.

4.3.2 Scattering Boundary Condition

In scattering problems, it is often of interest to simulate objects embedded in infinite space. Since infinite space cannot be simulated explicitly, *open* boundaries are needed. One approach to obtain such behavior is the *scattering boundary condition* (SBC). As an example, consider a plane wave propagating along the z-direction incident upon a planar boundary in the xy-plane. Since the normal derivative

$$\frac{\partial}{\partial z}\mathbf{E}(\mathbf{r}) = ik_z\mathbf{E}(\mathbf{r}) \tag{4.9}$$

is known at all points of the boundary, an exact BC can be applied. However, the unknown scattered field is rarely a plane wave propagating in a particular direction. Setting $\theta = 0$, an approximate condition is obtained

$$\frac{\partial}{\partial z}\mathbf{E}(\mathbf{r}) \approx i\tilde{n}k_0\mathbf{E}(\mathbf{r}). \tag{4.10}$$

This is the *first order* SBC for planar boundaries. It absorbs normally incident plane waves perfectly, but as θ increases the absorption decreases. At grazing incidence, all light is reflected. Higher order SBCs and SBCs for other types of surfaces can be constructed by requiring the field to (approximately) satisfy the *Sommerfeld radition condition* [24]. Details on such derivations are found e.g. in [22]. In the models considered in this work, only the first order SBC for planer surfaces has been used. While a second order SBC is available in COMSOL, the first order implementation was found to provide the best stability for the problems considered.

4.3.3 Perfectly Matched Layer

Like the SBC, the perfectly matched layer (PML) is a construction designed to emulate an open boundary. However, the PML is not an actual BC, but rather a fictitious absorber with a perfectly matched interface. Mathematically, the PML can be interpreted as a coordinate stretching in complex space [25], physically as an anisotropic absorber [26]. In continuum space, the interface matching ensures zero reflection for any plane wave, independent of incidence angle. Upon entering the PML, the wave is attenuated in the direction normal to the PML surface implying that back reflections are avoided (provided that the PML is thick enough). In continuum space, the PML is thus truly reflectionless, but unfortunately this property does carry over to discretized space [22]. Since numerical methods (like FEM) work in discretized space, PMLs will not be reflectionless, but they are still one of the best options. In particular, the combination of a PML and a SBC will result in low reflections across a wide range of angles. The trade-off compared to just using a SBC is that the PML must be meshed, e.g. the domain size is increased. In the simulations in this work a PML thickness of $\sim \lambda/2$ was found to be sufficient.

4.3.4 Wave port

In the full field formulation, the excitation must be supplied through a BC, when no external charge/current densities are present. An example of a BC providing such excitation is the *wave port*. Consider a wave port parallel to the xy-plane located at $z = z_0$. The excitation will be in the form of a plane wave propagating in the $+$z direction. Assuming that the port is located sufficiently far away from the structure of interest, higher-order modes are attenuated and only the dominant reflected mode reaches to port. In this case, the total field at the port can be expressed as

$$\mathbf{E}(\mathbf{r}) = \mathbf{E}_f e^{i\mathbf{k}_f \cdot \mathbf{r}} + \mathbf{E}_b e^{i\mathbf{k}_b \cdot \mathbf{r}} \tag{4.11}$$

where the first term represents the excitation and the second term the reflected wave. The normal derivative can be expressed as

$$\frac{\partial \mathbf{E}(\mathbf{r})}{\partial z} = i\tilde{n}k_0 \left(\mathbf{E}_f e^{i\mathbf{k}_f \cdot \mathbf{r}} - \mathbf{E}_b e^{i\mathbf{k}_b \cdot \mathbf{r}} \right) = -i\tilde{n}k_0 \left(\mathbf{E}(\mathbf{r}) - 2\mathbf{E}_f e^{i\mathbf{k}_f \cdot \mathbf{r}} \right), \tag{4.12}$$

which can be enforced as a BC. Equation (4.12) is a simple example of an *input port*. An *output port* can be constructed simply by setting $\mathbf{E}_f = 0$. The usage of the port condition equation (4.12) is limited by the assumption of higher-order modes being attenuated. However, the condition can be extended to include higher-order modes, provided that their form is known in advance [22].

4.4 Probes

The immediate result of a FEM calculation is the field distribution across the entire geometry. This result is typically too large to save directly, so instead the quantities of interest are "measured" using *probes*. Examples of probes are reflection/transmission coefficients

$$R = 1 - \frac{1}{P_0} \int_{\Omega_{inc}} (\langle \mathbf{S} \rangle \cdot \hat{\mathbf{n}}) \, \mathrm{dA}, \quad T = \frac{1}{P_0} \int_{\Omega_{out}} (\langle \mathbf{S} \rangle \cdot \hat{\mathbf{n}}) \, \mathrm{dA} \tag{4.13}$$

where $\Omega_{inc}/\Omega_{out}$ denote incoming/outgoing surfaces to which $\hat{\mathbf{n}}$ is a normal vector, $\langle \mathbf{S} \rangle$ is the time averaged poynting vector and P_0 the power incident through Ω_{inc}. For plasmonic particles the absorption, extinction and scattering cross sections are probed,

$$\sigma_{sct} = \frac{1}{I_0} \int_{\delta V} (\langle \mathbf{S}_{rel} \rangle \cdot \hat{\mathbf{n}}) \, \mathrm{dA}, \quad \sigma_{abs} = \frac{1}{I_0} \int_V Q_h \mathrm{dV}, \quad \sigma_{ext} = \sigma_{sct} + \sigma_{abs}. \tag{4.14}$$

Here V denotes the volume of the particle, δV the surface, $\langle \mathbf{S}_{rel} \rangle$ the relative, time averaged poynting vector and Q_h the power dissipation density. In the scattered field formulation $\langle \mathbf{S}_{rel} \rangle$ is simply the time averaged poynting vector calculated for the scattered field.

4.5 Implementation

Implementing a full FEM code is a complex and time demanding task. While open source projects exist that address this challenge, e.g. FEniCS [27], their accessibly and/or flexibility remains inferior to commercial software. In this work the COMSOL Multiphysics software [28] was used for all FEM calculations.

5 | Results

While most of the initial work have been of an explorative nature, e.g. setting up simulation environments and validating calculations for simple structures, some simulations of real structures have been carried out. Due to space limitations, all cannot be presented here. Instead, two examples have been selected based on the state of progression in terms of publication(s). The first example considers the light trapping properties of *nanowrinkles* for which the first paper has been submitted [31] and a number of additional papers are in preparation. In the second example a new *two particle model* for simulating random arrays of plasmonic nanoparticles is presented. A paper on upconversion applying the "old" one particle method has been already accepted [32], and the first SunTune paper of my own will be on the two particle model.

5.1 Nanowrinkles

When designing a solar cell reducing the thickness of the absorber implies lower material costs and shorter deposition times [30] thus decreasing the overall cost. The drawback is reduced absorption. This problem can be addressed by *light trapping*. As the wording suggests, the idea is to trap the light inside the structure. Since the light cannot (or only rarely) escape, it bounces around passing the absorber layer multiple times increasing the effective path length and thereby the absorption. Light trapping can be achieved by fabricating the solar cell on top of a textured substrate. The fabrication of precisely controlled textures on nanoscale, e.g. by electron beam lithography (EBL), is an expensive process with a low throughput. A cheaper alternative is self assembled nanostructures such as nanowrinkles, which can be fabricated as illustrated in figure 5.1. Since the

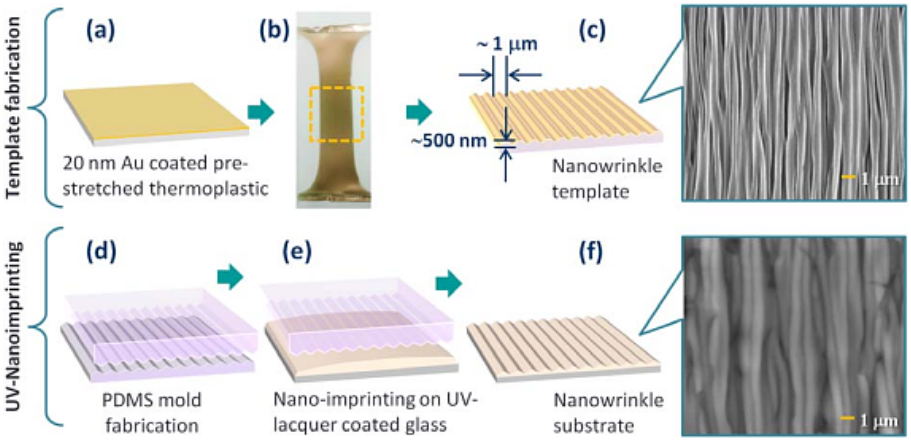

Figure 5.1: Fabrication of nanowrinkles. First, a thin gold film is deposited on pre-stretched thermoplastic (a), which is subsequently clamped and annealed above the glass transition temperature (b) so that nanowrinkles form on the surface (c). Next, a PDMS mold (d) is used to transfer the wrinkles to a UV-lacquer coated glass (e), which will serve as the solar cell substrate (f). Reproduced from [31].

manufacturing process is simple and requires no expensive equipment, the production of nanowrinkles is cheap and easily scalable. Furthermore, the size of the nanowrinkles can be tuned, e.g. by varying the gold layer thickness. In an upcoming publication [31] the light trapping performance of the nanowrinkles shown in figure 5.2 is assessed.

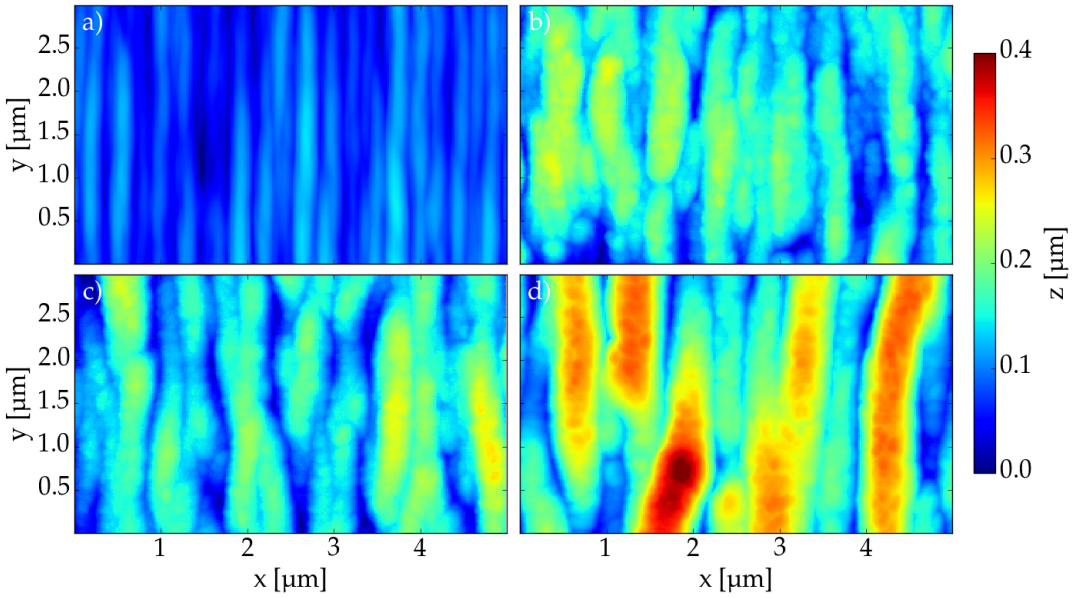

Figure 5.2: Topology of the surface of four nanowrinkle samples measured by Atomic-Force Microscopy (AFM). The size of the nanowrinkles was varied by changing the thickness of the gold layer from 5 nm (a) to 10 nm (b), 15 nm (c) and 20 nm (d). Accordingly the samples are denoted NW5, NW10, NW15 and NW20.

5.1.1 Model

The geometrical model of the nanowrinkle structure was created by stacking the layers conformally. The cross sectional FIB SEM images (shown for the NW20 sample in figure 5.3a) confirm that this assumption is reasonable. The surface template was taken as a 2D slice through the corresponding AFM measurement. A 2D (rather than 3D) model was chosen to limit computation time and memory consumption. The resulting 2D geometry is shown in figure 5.3b.

To emulate the quasi periodic nature of the surface, a number of separate simulations with periodic BCs were carried out with different surface templates, and the target variables

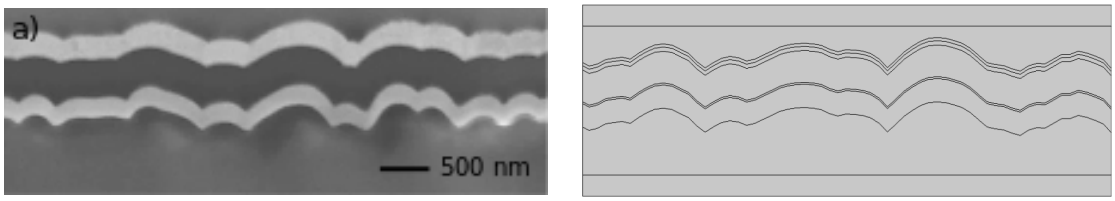

(a) FIB image reproduced from [31].

(b) Conformal model geometry.

Figure 5.3: Geometry of the NW20 sample. The slices in (a), (b) are not the same.

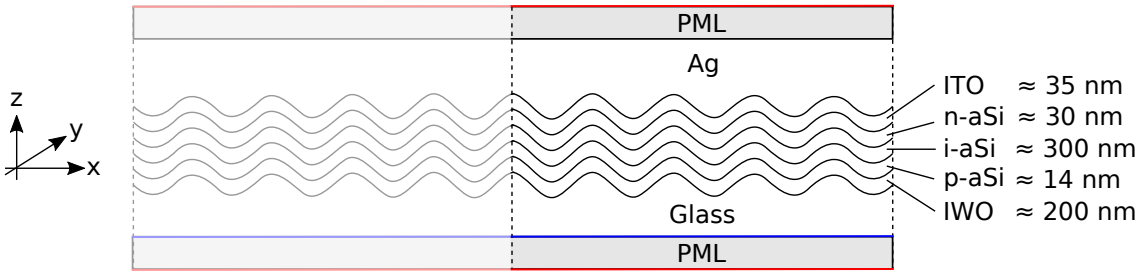

Figure 5.4: Sketch of the FEM model. To obtain a symmetric structure, the initial structure is mirrored in the z-axis. Applying appropriate PECs/PMCs (dashed lines), the simulation domain is reduced to the non-shaded area. The top and bottom of the structure is truncated by PMLs backed by SBCs (red lines) to avoid unintended reflections. The structure is excited by a monochromatic plane wave propagating in the positive z-direction using a wave port BC (blue line).

were calculated as the mean across all simulations. To obtain a broadband spectrum, simulations were carried out in steps of 2 nm from 300–900 nm. The resulting data were smoothed using a Gaussian kernel corresponding to a coherence length of 20 μm to filter out diffraction effects, as discussed in section 3.3.2. The FEM model is sketched in figure 5.4.

5.1.2 Results

The simulated spectra are compared to the measured ones in figure 5.6. For the flat solar cell, the agreement is good. The slight discrepancy between model and experiment can be attributed to production uncertainties (layer thicknesses/uniformity) and variations in material parameters (the complex refractive index). The refractive indexes were measure by ellipsometry for all materials except silver, which was taken from the literature. Overall, the simulated data for the NW5 sample are also in reasonable agreement with simulation. However, the measured peak locations differ somewhat from the simulated ones, implying that the layer thicknesses used in the simulation might be inaccurate. In case of the NW20 sample, the general tendency of increased absorption for long wavelenghts ($\lambda > 600$ nm) is predicted by the model, but the measured absorption is much higher than predicted. Besides non-idealities in the simulation parameters, a possible explanation could be additional scattering not accounted for by the model due to the non-uniformity of the nanowrinkles in the y-direction. Since the simulations are carried out in 2D (xz-plane), the nanowrinkles are implicitly assumed to be perfectly homogeneous in the y-direction.

The spatial power dissipation density is illustrated in figure 5.6 for different wavelengths. At the lowest wavelength ($\lambda = 475$ nm) all the light is absorbed in the intrinsic silicon layer before reaching the back reflector. As the wavelength increases, the extinction coefficient of silicon decreases, and the light trapping caused by the nanowrinkles becomes more important. At highest wavelength ($\lambda = 775$ nm) only very weak absorption is observed in the flat sample. In the nanowrinkle sample on the other hand, hot-spots of high absorption are distributed across the sample. The hot-spots cause an overall increased absorption compared to the flat cell in agreement with figure 5.5.

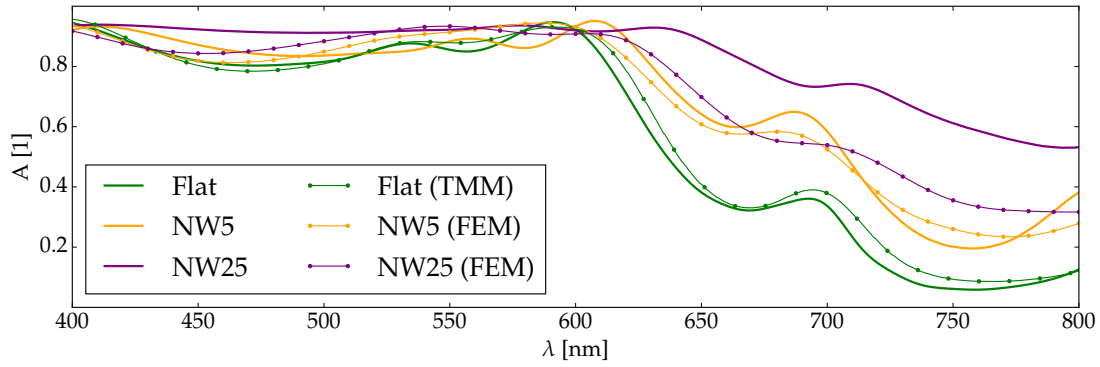

Figure 5.5: Comparison of measured (solid lines) and simulated data (lines + dots). For the nanowrinkle samples, the polarization average is plotted.

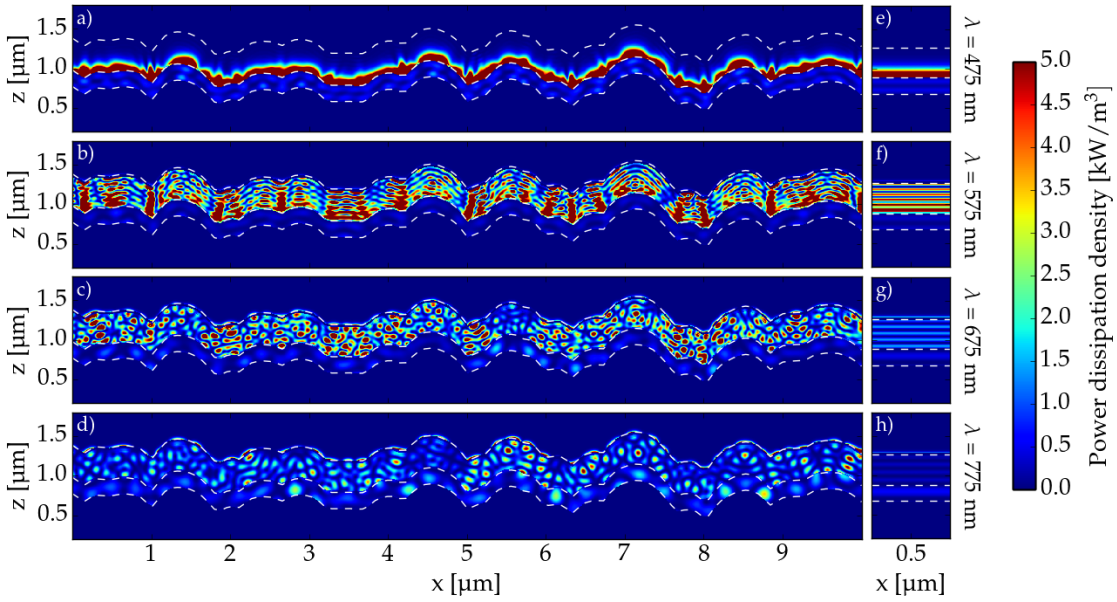

Figure 5.6: Power dissipation density in the NW20 (a-d) and the flat (e-h) solar cells. The light is incident along the positive z-direction, e.g. from below. The dashed white lines indicate the interfaces between (from below) glass/IWO, IWO/silicon and ITO/silver.

5.1.3 Outlook

An obvious extension of this work would be to construct a 3D model of the nanowrinkle sample(s) to assess the effect of non-uniformity in the y-direction. To limit the need for computational resources, the 3D model could be evaluated on a smaller domain, maybe $2.5 \times 2.5\ \mu\text{m}^2$, and, as a starting point, at a single wavelength.

In other upcoming papers the angular dependence of the absorption is considered in detail. For these papers it would be natural to carry out the corresponding calculations at oblique incidence. At oblique incidence the symmetries exploited so far will no longer be present. Revoking the PEC/PMC BC along the z-axis and replacing the outer PEC/PMC BCs by flouqet BCs, simulations at oblique incidence can be carried out.

5.2 The two particle model

For a random arrangement of plasmonic metal nanoparticles, the average particle-particle coupling will be small provided that the mean center-to-center distance is large enough. In this quasi-single particle case, an approximate result can be obtained by considering a single particle alone in infinite space. The simplicity of this *one particle model* combined with its ability to predict main trends has made it a popular choice [7]. In a recent SunTune paper on plasmonically enhanced upconversion [32], the one particle model was used to predict the position of the plasmon resonance for randomly distributed truncated gold nanocones on a TiO_2 film on a SiO_2 substrate. While it succeeded in predicting the main trends, some features, in particular a peak splitting behavior, remained unaccounted for. In an upcoming paper, an extension of the one particle model with an additional particle, e.g. a *two particle model*, will be proposed as an improved approximation taking into account the nearest-neighbor particle-particle interaction.

The models are compared to experimental data previously published in [32]. The samples were fabricated on a quartz substrate onto which a 100 nm film of TiO_2:Er^{3+} was deposited by radio-frequency magnetron sputtering. The gold cylinders were fabricated on top of the film by EBL in 2×2 mm^2 regions. Three series of samples were fabricated. The sets are named S4k, S6k and S8k according to their particle density of 4000, 6000, and 8000 particles per 100×100 μm^2. SEM images of a sample from each series are shown in figure 5.7a-c. The particle height was 50 nm for all samples. A TEM image of a fabricated particle is shown in figure 5.7d.

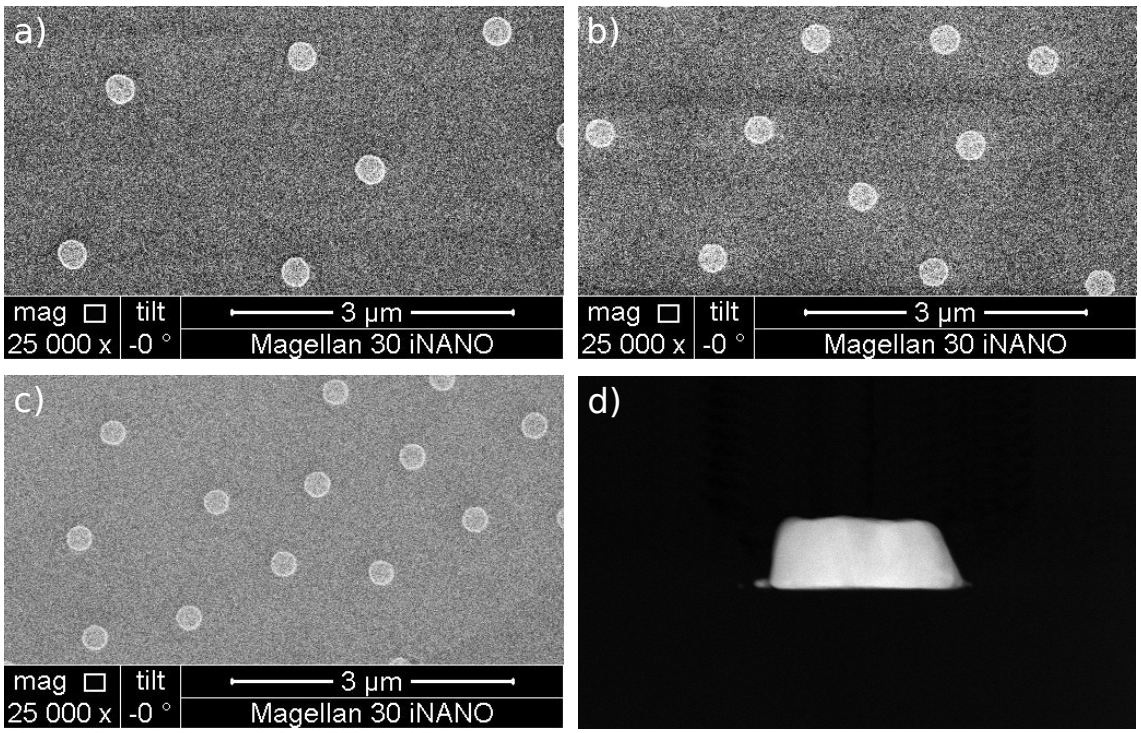

Figure 5.7: SEM images of a samples from each series, S4k (a), S6k (b) and S8k (c). TEM image of a gold nanoparticle with a diameter of 147 nm (d).

5.2.1 Models

The model geometry was constructed as simple planar layers with the gold nanoparticle(s) on top. The nanoparticle is modeled as a truncated cone with top radius 0.9 times the bottom radius in qualitative agreement with the TEM image, figure 5.7d. A sketch of the FEM model is shown in figure 5.8. Since the analytical solution for the structure in the absence of the nanoparticle(s) is known, the scattered field formulation was used. The background field was evaluated using TMM and injected into COMSOL through a custom interface, *tmmpy_bridge*, which was created as part of this work.

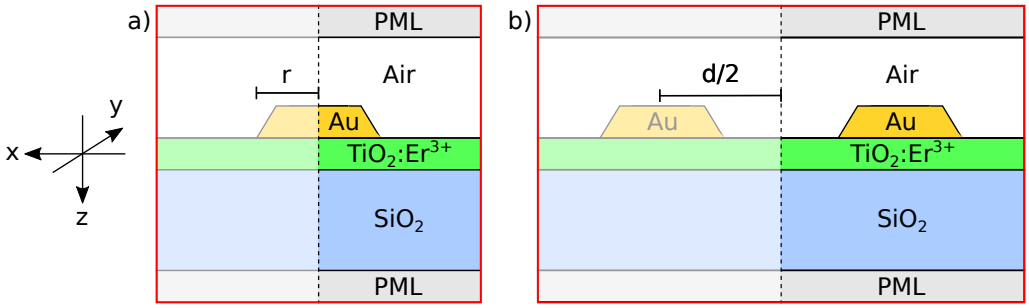

Figure 5.8: Sketch of the FEM model for (a) the one particle model and (b) the two particle model. The particle radius r and center-to-center distance d (only relevant for the two particle model) are indicated. The red boundaries indicate SBCs. Applying an appropriate BC (PEC/PMC) along the symmetry axis (dashed line), the simulation domain is reduced to the non-shaded region.

5.2.2 Model comparison

For the model comparison, a particle with $r = 135$ nm was chosen. Calculated extinction cross section spectra for the one particle model and two particle models with different center-to-center distances d are compared in figure 5.9 for the case of s-polarization, e.g. the electric field is perpendicular to axis connecting the two particles. For p-polarization, no significant coupling is observed. When d is small, the plasmonic peak is blueshifted, but as d increases the blueshift decreases until the peak is aligned with the one particle peak at $d \approx 580$ nm. Next, the peak is redshifted and around $d \approx 900$ nm a new, blueshifted peak is formed while the amplitude of the redshifted peak decreases. At $d \approx 1100$ nm, the amplitudes of the two peaks are similar in magnitude. Upon increasing d further, the redshifted peak dies out, and the previous peaks movements repeat periodically while simultaneously the curve converges towards the one particle model curve.

To illustrate the significance of the values of d where a resonance sharpening/splitting is observed, the phase difference between the background field and the scattered field emitted by a single particle is plotted in figure 5.10. From the phase plot it is clear that the peak sharpening occurs when the second particle is placed close to the zero phase shift line, e.g. where the background field and the scattered field interfere constructively. Similarly, the peak splitting occurs when the second particle is placed close to the π phase shift line, e.g. when the background field and the scattered field interfere destructively. Admittedly the agreement is not perfect (the particle positions are not *exactly* on the $0/\pi$ lines). However, a perfect agreement was not expected either. The interference condi-

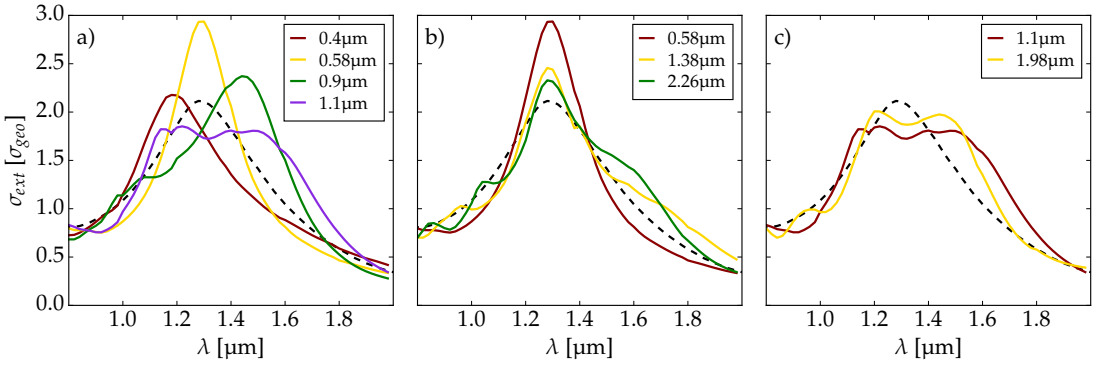

Figure 5.9: Comparison of one (dashed line) and two (solid lines) particle models for different particle separations (a). At some distances a sharpening of the resonance is observed (b), while at others the resonance peak splits into two (c).

tions based on a single particle simulation does not take into account any particle-particle coupling effects, so some deviation is expected. On the other hand, the qualitative agreement imply that the peak splitting/sharpening is primarily due to the radiative coupling between neighboring particles and the incoming field. This conclusion is similar to the observations by [4].

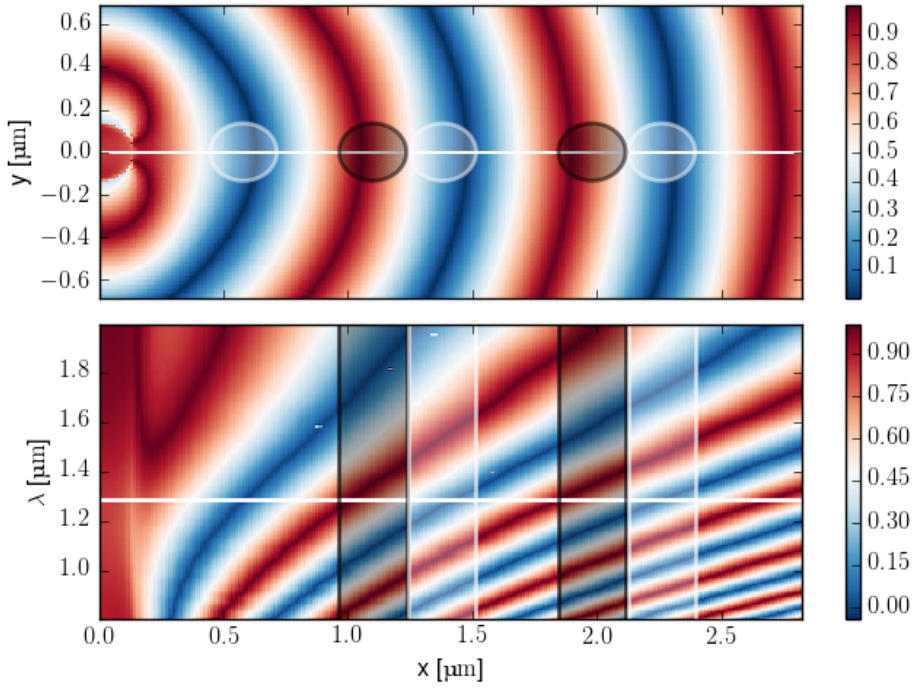

Figure 5.10: Phase difference between the y-component of background field and the scattered field in units of π in space for z=0, $\lambda = 1290$ nm (upper panel) and as a function of excitation wavelength for z=y=0 (lower panel). The data in the upper/lower panels coincide along the white, horizontal lines. White/black shadings indicate particle positions for which peak sharpening/splitting is observed in the two-particle simulations.

5.2.3 Results

In figure 5.11a-c the extinction cross sections calculated using the one and two particle models respectively are compared to experimental data. To highlight the difference between the two models, the two particle model results are shown for s-polarization rather than a polarization average. For each sample series, d was chosen as the mean particle distance. The peak splitting observed experimentally is reproduced neatly by the two particle model. While the curves do not match perfectly in absolute numbers (the vertical shift might be due to scattering effects which remain unaccounted for), the features on the experimental curves agree well with the two particle model. The fitted peak position(s) as a function of particle diameter is shown in figure 5.11d-f. Considering the simplicity of the two particle model, the agreement with the experimental data is remarkably good.

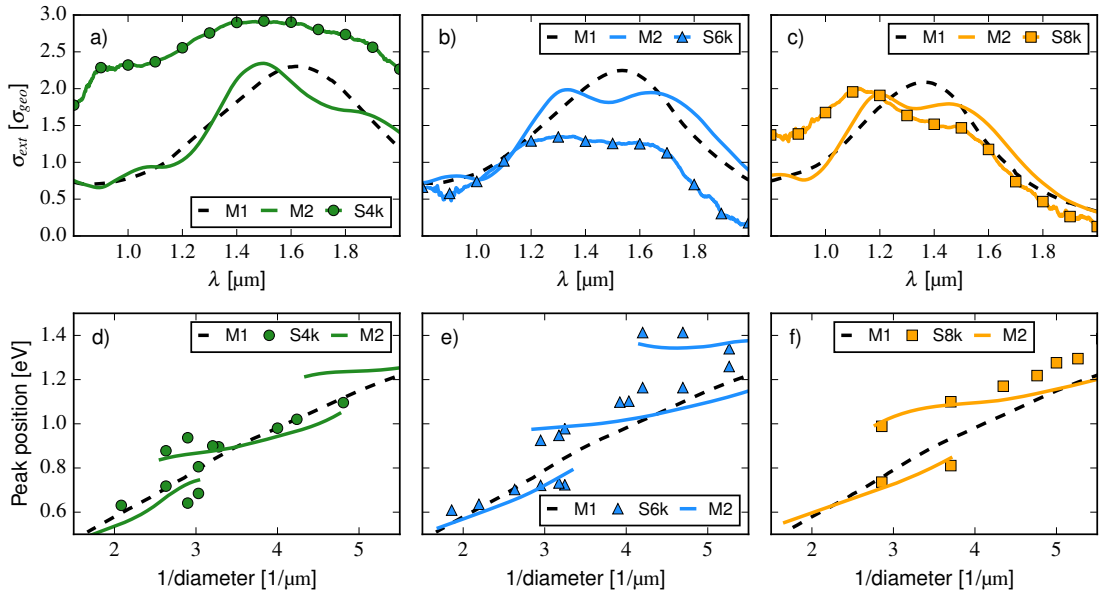

Figure 5.11: Comparison of one (M1, dashed line) and two (M2, solid lines) particle models with experimental data (symbols). In the upper panel, the samples considered are S4k with 345 nm diameter (a), S6k with 315 nm diameter (b) and S8k with 270 nm diameter (c). In the lower panel peak position(s) as a function of diameter are shown for the S4k (d), S6k (e) and S8k (f) samples.

5.2.4 Outlook

To obtain a better agreement with the experimental data, obvious extensions would be to take into account the actual particle distribution (or some approximation to it) rather than simply the mean distance and/or to consider polarization averaged calculations. It would also be very interesting to look at samples with larger values of d to verify experimentally if the peak splitting occurs periodically as predicted by the two particle model.

6 | Conclusion

Applying TMM and FEM, optical simulations have been carried out successfully for a number of different structures. A modeling framework has been developed which enable modeling of thin film structures by TMM (*tmmpy*) and provides integration with COMSOL (*tmmpy_bridge*), so that thin film structures with scattering elements can be treated with ease. Since this is exactly the type of structures typically encountered in SunTune, these tools provide a solid foundation for the construction of future optical models in SunTune regi.

6.1 Outlook

One of the main objectives of this PhD project is optical simulation of the complete solar cell complex, including any up- and downconverter elements. Since the complete geometry is too large to be treated using FEM directly, an alternative method must be applied. Some work has been done on a variation of TMM taking into account the angular intensity distribution building on the concepts of [13, 14]. The basic idea is to divide the complete structure into blocks, process each block by the most efficient method available (into some matrix representation), after which the blocks are assembled to determine the response of the complete structure. In future work, the method will be finalized and published in a separate paper.

While the simulation of periodic arrangements of nanoparticles is relatively straightforward (it is sufficient to treat a single unit cell), the problem of treating random arrangements is more involved. For prediction of the plasmonic resonance frequency, the random arrangement is often approximated by considering a single particle alone in the world. As an improved approximation, a two particle model was presented in section 5.2. In future work it would be interesting to consider alternative options for including more particles. One possible approach would be to expand the field around each particle in spherical vector wave functions (SVWFs), after which scattering from other identical particles can be included via the addition theorem for SVWFs. In recent publications, e.g. [33], this approach has been successfully applied to simulate thousands of particles.

A three month stay abroad at the Fraunhofer-Institut für Solare Energiesysteme (ISE) has been planned. A paper has previously been published from ISE on upconversion enhancement using a Bragg structure [34]. The initial work was focused on structures which could be manufactured in their lab. During my stay, I will be extending this work to more exotic structures. The focus will be on optimizing the upconversion quantum yield from a more theoretical point of view without taking into account immediate, experimental limitations. The expected outcome is a joint publication.

Bibliography

1. Green, M. A., Emery, K., Hishikawa, Y., Warta, W. & Dunlop, E. D. Solar cell efficiency tables (version 48). *Progress in Photovoltaics: Research and Applications* **24,** 905–913. ISSN: 1099-159X (2016).
2. Shockley, W. & Queisser, H. J. Detailed Balance Limit of Efficiency of p-n Junction Solar Cells. *Journal of Applied Physics* **32,** 510–519 (Mar. 1961).
3. Johannsen, S. R. *Upconversion of near-infrared light through Er doped TiO_2, and the effects of plasmonics and co- doping with Yb* PhD thesis (University of Aarhus, 2015).
4. Forestiere, C. *et al.* Genetically engineered plasmonic nanoarrays. *Nano letters* **12,** 2037–2044 (2012).
5. Mock, J., Barbic, M, Smith, D., Schultz, D. & Schultz, S. Shape effects in plasmon resonance of individual colloidal silver nanoparticles. *The Journal of Chemical Physics* **116,** 6755–6759 (2002).
6. Jensen, T. R. *et al.* Nanosphere lithography: effect of the external dielectric medium on the surface plasmon resonance spectrum of a periodic array of silver nanoparticles. *The Journal of Physical Chemistry B* **103,** 9846–9853 (1999).
7. Zorić, I., Zäch, M., Kasemo, B. & Langhammer, C. Gold, Platinum, and Aluminum Nanodisk Plasmons: Material Independence, Subradiance, and Damping Mechanisms. *ACS Nano* **5.** PMID: 21438568, 2535–2546 (2011).
8. Jensen, T. R., Malinsky, M. D., Haynes, C. L. & Van Duyne, R. P. Nanosphere lithography: tunable localized surface plasmon resonance spectra of silver nanoparticles. *The Journal of Physical Chemistry B* **104,** 10549–10556 (2000).
9. De Abajo, F. J. G. Microscopy: Plasmons go quantum. *Nature* **483,** 417–418. ISSN: 0028-0836 (2012).
10. Madsen, S. P. *et al.* Optimizing Plasmonically Enhanced Upconversion. *Energy Procedia* **77,** 478 –486. ISSN: 1876-6102 (2015).
11. Jackson, J. D. *Classical electrodynamics* 3rd ed. (Wiley, New York, NY, 1999).
12. Byrnes, S. J. Multilayer optical calculations. *ArXiv e-prints.* arXiv: 1603.02720 (2016).
13. Tucher, N. *et al.* 3D optical simulation formalism OPTOS for textured silicon solar cells. *Opt. Express* **23,** A1720–A1734 (2015).
14. Krč, J., Smole, F. & Topič, M. Analysis of light scattering in amorphous Si: H solar cells by a one-dimensional semi-coherent optical model. *Progress in photovoltaics: Research and Applications* **11,** 15–26 (2003).
15. Troparevsky, M. C., Sabau, A. S., Lupini, A. R. & Zhang, Z. Transfer-matrix formalism for the calculation of optical response in multilayer systems: from coherent to incoherent interference. *Opt. Express* **18,** 24715–24721 (2010).
16. Santbergen, R., Smets, A. H. & Zeman, M. Optical model for multilayer structures with coherent, partly coherent and incoherent layers. *Opt. Express* **21,** A262–A267 (2013).

17. Pedrotti, F. L., Pedrotti, L. M. & Pedrotti, L. S. *Introduction to Optics (3rd Edition)* 3rd ed. ISBN: 0131499335 (Addison-Wesley, Apr. 2006).

18. Sarrazin, M., Herman, A. & Deparis, O. First-principle calculation of solar cell efficiency under incoherent illumination. *Optics Express* **21,** A616 (July 2013).

19. Lee, W., Lee, S.-Y., Kim, J., Kim, S. C. & Lee, B. A numerical analysis of the effect of partially-coherent light in photovoltaic devices considering coherence length. *Opt. Express* **20,** A941–A953 (2012).

20. Centurioni, E. Generalized matrix method for calculation of internal light energy flux in mixed coherent and incoherent multilayers. *Appl. Opt.* **44,** 7532–7539 (2005).

21. Larson, M. G. & Bengzon, F. *The Finite Element Method: Theory, Implementation, and Applications* ISBN: 3642332862, 9783642332869 (Springer Publishing Company, Incorporated, 2013).

22. Jin, J.-M. *The finite element method in electromagnetics* (John Wiley & Sons, 2014).

23. Whaley, R. C. & Petitet, A. Minimizing development and maintenance costs in supporting persistently optimized BLAS. *Software: Practice and Experience* **35,** 101–121 (2005).

24. Schot, S. H. Eighty years of Sommerfeld's radiation condition. *Historia Mathematica* **19,** 385 –401. ISSN: 0315-0860 (1992).

25. Chew, W. C. & Weedon, W. H. A 3D perfectly matched medium from modified Maxwell's equations with stretched coordinates. *Microwave and optical technology letters* **7,** 599–604 (1994).

26. Sacks, Z. S., Kingsland, D. M., Lee, R. & Lee, J.-F. A perfectly matched anisotropic absorber for use as an absorbing boundary condition. *IEEE transactions on Antennas and Propagation* **43,** 1460–1463 (1995).

27. Alnæs, M. S. *et al.* The FEniCS Project Version 1.5. *Archive of Numerical Software* **3** (2015).

28. COMSOL AB, Stockholm, Sweden. *COMSOL Multiphysics* version 5.2a. 2016.

29. Desta, D. *et al. Photovoltaic-Performance-Enhancing Patch with Combined Light Trapping and Spectral Upconverting Effect* in *EU PVSEC Conference Proceedings* (2016).

30. Haug, F.-J. & Ballif, C. Light management in thin film silicon solar cells. *Energy Environ. Sci.* **8,** 824–837 (3 2015).

31. Ram, S. K. *et al.* Light-trapping properties of quasi-periodic uniaxial nanowrinkle surface for thin film silicon solar cells. *ACS Nano* (expected 2017).

32. Lakhotiya, H. *et al.* Plasmonically enhanced upconversion of 1500 nm light via trivalent Er in a TiO2 matrix. *APL* (2017).

33. Lai, J., Kobayashi, M. & Barnett, A. A fast and robust solver for the scattering from a layered periodic structure containing multi-particle inclusions. *Journal of Computational Physics* **298,** 194 –208. ISSN: 0021-9991 (2015).

34. Hofmann, C. L. M., Herter, B., Fischer, S., Gutmann, J. & Goldschmidt, J. C. Upconversion in a Bragg structure: photonic effects of a modified local density of states and irradiance on luminescence and upconversion quantum yield. *Opt. Express* **24,** 14895–14914 (2016).